ELECTROCHEMISTRY

Designing interphases for practical aqueous zinc flow batteries with high power density and high areal capacity

Shuo Jin[1]†, Yiqi Shao[1]†, Xiaosi Gao[1], Pengyu Chen[1], Jingxu Zheng[2], Shifeng Hong[2], Jiefu Yin[1], Yong Lak Joo[1]*, Lynden A. Archer[1]*

Aqueous zinc flow batteries (AZFBs) with high power density and high areal capacity are attractive, both in terms of cost and safety. A number of fundamental challenges associated with out-of-plane growth and undesirable side reactions on the anode side, as well as sluggish reaction kinetics and active material loss on the cathode side, limit practical deployment of these batteries. We investigated artificial interphases created using a simple electrospray methodology as a strategy for addressing each of these challenges. The effectiveness of the electrospray interphases in full cell zinc-iodine flow batteries was evaluated and reported; it is possible to simultaneously achieve high power density [115 milliwatts per square centimeter (mW/cm^2)] and high areal capacity [25 milliampere hour per square centimeter (mA·hour/cm^2)]. Last, we extended it to aqueous zinc-bromine and zinc-vanadium flow batteries of contemporary interest. It is again found that high power density (255 and 260 mW/cm^2, respectively) and high areal capacity (20 mA·hour/cm^2) can be simultaneously achieved in AZFBs.

INTRODUCTION

Energy storage technologies, such as lithium (Li) batteries (*1*), fuel cells (*2*), and flow batteries (*3*), have attracted substantial research and public attention recently. While some of this attention reflects the emergence of electrical energy storage (EES) as an enabling technology in multiple sectors, a substantial component stems from the still largely unmet market demand for EES technologies that can achieve the scale and cost characteristics required under the emergent "electrify everything" scenario demanded to meaningfully lower humanity's rising greenhouse gas emissions. During the past 20 years, Li-ion batteries (LIBs) have emerged as a promising, even market-dominant technology platform because of their versatility and relative maturity of knowledge of the enabling chemistry-, cell-, manufacturing-, and system-level aspects (*4*). Intrinsic challenges ranging from the flammability of the most promising organic electrolytes, limited energy density, and relatively high cost per kilowatt-hour of stored energy have motivated a large volume of application-focused and fundamentally focused work to identify safer and more economical substitutes (*5*, *6*). Among these efforts, Li metal batteries (*7*) have received notable attention because they preserve many of the key attributes of the LIB (e.g., cathodes able to host Li with high levels of reversibility, high operating voltages, etc.), and because of high theoretical specific capacity of Li, 3860 mA·hour/g, they can offer potential to achieve battery cells with higher specific energies. Unfortunately, these and other benefits come with their own challenges related to safety, cost, and battery lifetime (*8*).

Aqueous rechargeable zinc (Zn) batteries have long been known to provide an important alternative EES technology in settings (e.g., large-scale storage inside residences and buildings, fully autonomous robots, etc.) where reliability and unquestionable safety are required

(*9*). According to the 2022 real-time transaction data (*10*), the price of Zn is 3.75 USD/kg, around 18 times lower than that of Li (68.10 USD/kg), illustrating the promise of Zn batteries as cost-effective alternatives to market-dominant Li battery technology. A large number of aqueous Zn battery concepts (*11*), such as Zn-MnO$_2$ (*12*), Zn-NiOOH (*13*), Zn-air (*14*), and aqueous Zn flow batteries (AZFBs), in which the aqueous electrolyte is flowing through the electrode, have consequently emerged and demonstrated to offer practical advantages in terms of high capacity and high power density, enabling the flow battery system to be a promising economic large-scale energy storage system (*13*, *15*–*18*). Here, we focused on Zn flow batteries because, compared with conventionally closed battery cells where capacity is limited by the electrode materials and power is limited by intrinsic transport processes, the flow battery provides multiple degrees of freedom for achieving increased storage capacity and power, which are now considered essential for the design of the large-scale EES systems appropriate for managing intermittency and seasonality of energy supplies from wind power and solar photovoltaics installations. AZFBs will be shown herein to provide a powerful platform for fundamental materials and application-focused innovations to meet these needs.

To more concretely define the open technical questions and achieve high power and high energy in practical AZFBs, we will focus on our recently reported finding of using an AZFB to power energy-dense swimming robots with an electrolytic vascular system (*19*). A unique feature of these battery systems is that the flowing electrolyte serves two functions—it serves both as an essential requirement for high-power storage and as an actuation fluid that drives the swimming motion of the robot. Power density limited by the energy output per area (discharge voltage × current density) determines the highest swim speed of the robot—the higher the power density, the faster the robot swims. On the other hand, areal capacity evaluated by the stored energy for each charge decides how long the robot can operate without interruption. Hence, achieving high power density and high areal capacity simultaneously is a requirement.

The key technical challenges to achieving both requirements are related to (i) controlling the interfacial reaction and adsorption rates;

[1]Robert Frederick Smith School of Chemical and Biomolecular Engineering, Cornell University, Ithaca, NY 14853, USA. [2]Department of Materials Science and Engineering, Cornell University, Ithaca, NY 14853, USA.
*Corresponding author. Email: ylj2@cornell.edu (Y.L.J.); laa25@cornell.edu (L.A.A.)
†These authors contributed equally to this work.

(ii) preventing mossy/dendritic Zn growth during recharge; (iii) minimizing parasitic redox reactions and side products, which can passivate the electrodes; and (iv) limiting/eliminating gas evolution produced by water splitting (Fig. 1) (20–22). For instance, to achieve high power density, a high average discharge voltage must be maintained under high current density. Fundamentally, high average discharge voltage means that interfacial diffusion kinetics and reaction kinetics need to be improved to stabilize the interfacial ion concentration gradient, and high current density means that serious side reactions and unregulated reaction rate need to be suppressed. In addition to that, high areal capacity also introduces dendrite problems for zinc sides (23, 24) and "ion crossover" problems for cathode side (25). Hence, to improve the overall performance of AZFBs with high power density and areal capacity, several problems posed by the high current density and high areal capacity need to be considered. First, as Fig. 1 shows, for zinc electrodeposition at the anode side, strong interfacial reaction rate resulting from high current density drives the fast growth rate of Zn dendrite, which readily short-circuits the battery or leads to the formation of "orphaned zinc" and poor reversibility (26). In addition, because of the close reduction potential between zinc ions and hydrogen ions (27), hydrogen evolution reaction (HER) is aggravated under high current density, which results in (i) the low coulombic efficiency (CE) of reversible Zn electrodeposition and (ii) formation of side product ZnO, the nonconductive nature of which has a negative influence on the electrodeposition morphology and efficiency. Next, for cathode side, the slow reaction kinetics and weak adsorption ability stress the importance of interfacial engineering to accommodate the superfast reaction rate (28). Otherwise, the serious ion crossover either covers the whole Nafion membrane, highly decreasing the ion conductivity, or mixes with the anode electrolyte leading to the failure of the battery. As a final point, the ionic conductivity of the membrane has a rather large effect on the energy efficiency of the battery cell (15, 29). With high ion conductivity, the mass transport potential decreases, and the energy efficiency increases.

With the specific aim of innovating practical, cost-effective AZFB systems that offer high power, high energy, and long life, inexpensive materials are preferred (9). On this basis, effective and low-cost materials will be the first choice for our validation. Second, for the zinc electrodeposition process, interfacial metal-substrate bonding has been reported to be effective in our previous works (30), especially under high current density and areal capacity. For example, epitaxy growth of Zn crystals has high reversibility by aligned graphene layers (23), which can be selected to construct the interfacial metal-substrate bonding to stabilize the zinc electrodeposition. Third, to stress the importance of the interfacial reaction and adsorption process at the cathode side, inexpensive materials such as activated carbon (AC) [0.111 USD/kg; Silicon Products (P) Associates] (31) with high surface area are chosen here to improve the interfacial properties. With strong adsorption ability of AC, both reactant and products can be fixed at the cathode surface, which is beneficial for interfacial kinetics. Significantly, for three-dimensional (3D) electrode structure of the flow battery electrodes, unlike 2D electrode, conformal and controllable coating process is much harder to achieve. Taking aligned graphene as an example, graphene layers can be aligned using doctor blades for 2D electrodes, which is impossible for 3D electrodes. Although chemical vapor deposition (32) and atomic layer deposition (33) are possible choices for 3D electrode interfacial engineering, the high cost of these processes hinders the application in AZFBs. Considering large-scale application and expense, electrospray (34), which is a mature industrial technology, is singled out as a good candidate for 3D electrode interfacial engineering work. We have added high-speed air through the sheath layer of the coaxial nozzle system of our air-controlled electrospray to synergistically combine
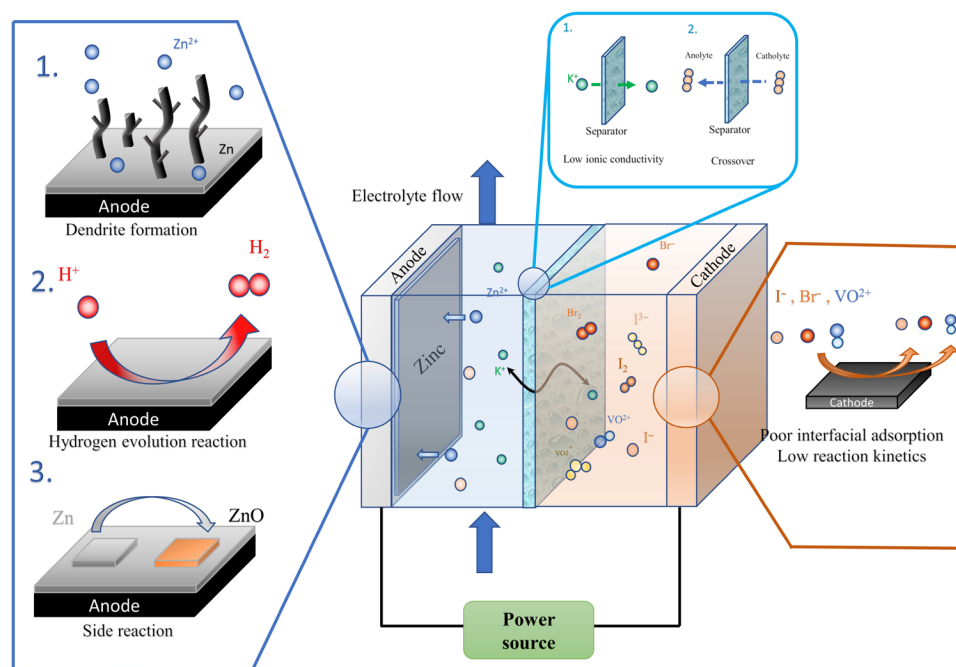
Fig. 1. Fundamental barriers for practical AZFBs. Schematic illustrating the fundamental barriers to fast-charging practical AZFBs, which are addressed in the present study.

high-speed air and high electric force as driving forces, which has shown to be very effective in controlling the assembly of 2D materials such as graphene in various battery electrode applications (*35, 36*). Relying on the strong electrostatic force and high-speed air flow, the graphene layer can be aligned, and the interfacial coating process for both anode and cathode sides is more controllable. On the basis of all these requirements and chosen materials, we first choose an aqueous Zn-iodine flow battery as an example to prove our designing principles and interfacial engineering works and then extend this interfacial engineering work into other AZFBs, such as Zn-bromine and Zn-vanadium batteries. Notably, these interfacial engineering processes are general to most AZFB systems and can achieve high power density ($115 mW/cm^2$ for Zn-iodine flow batteries, $255 mW/cm^2$ for Zn-bromine flow batteries, and $260 mW/cm^2$ for Zn-vanadium flow batteries), areal capacity, and long cycling performance for all validation models (Fig. 2) (*16, 25, 28, 37–41*). Our interfacial engineering works, therefore, provide an exciting pathway toward low-cost and large-scale storage of electrical energy.

RESULTS

Creating aligned graphene by electrospray

Nonuniform zinc electrodeposition leads to the formation of mossy/dendritic deposition, ultimately leading to battery failure by a number of processes, including shorting, orphaned zinc, and electrode passivation due to the formation of insulating side products (ZnO), especially at high current density (*9, 39*). To overcome these problems, interfacial metal-substrate bonding, such as Zn-graphene bonding, which can provide a high chemical potential for the zinc nucleation process is a potential method (*30*). Here, strong interfacial Zn^{2+} reduction process can be regulated by the zinc crystal epitaxy growth process enabled by well-aligned graphene layers (Fig. 3A), in which epitaxy growth can provide high nucleation chemical potential. Aligning graphene layers conformally on the surface of a 3D electrode, such as carbon felt (CF), is generally a difficult process, especially when the goal is to achieve controllable, aligned graphene layers. Hence, we used electrostatic force to align the graphene layers (Fig. 3A), and by doing this, the amount of graphene can be determined by

Fig. 2. Power density and areal capacity achieved in this work. Comparison of the power density and areal capacity achieved in various AZFB systems reported in this work, compared to the respective state-of-the-art performance reported in contemporary literature studies.

controlling the electrospraying time and flow rate, meaning that thin aligned graphene layers can be achieved. Compared with the doctor-blade shear graphene (DG) coating process, electrospray graphene (EG) can be better controlled in terms of orientation and amount. As x-ray diffraction (XRD) (Fig. 3B) shows, thin aligned EG layers only show the (002) plane, which is different from the DG layers that show the small intensity of the (101) plane and (004) plane, indicating the better-aligned effect by electrostatic force. The full width at half maximum (FWHM) decreases with EG (FWHM, 0.24), further proving the better-aligned crystalline states compared with DG (FWHM, 0.45) (*42*). The shift of (002) plane should result from the strong electrostatic force applied to the graphene layer. The Raman spectrum (Fig. 3C) can further prove this result: Band D shows the degree of defects of the graphene layers, meaning that the higher intensity the band D has, the more defects the graphene layers have (*43, 44*). As Fig. 3C depicts, the ratio between bands D and G decreases, indicating that the graphene layers are better aligned (parallel to the substrate) with fewer defects by electrostatic force. The morphology of the DG layers in the large-scale CF (DG@CF) shows that DG only covers the surface of the CF, which means that it does not immerse into the 3D carbon fiber structure (fig. S1). Furthermore, the porous structure of the 3D CF, which provides space for the flowing electrolyte, is blocked by the DG (fig. S1). In stark contrast, the morphology of the EG layers in CF (EG@CF) is smooth and uniform at each 3D carbon fiber (fig. S1). Moreover, the porous structure of 3D CF is not affected by the smooth thin EG layers. Thus, it is concluded that the 3D aligned graphene coating layers can be achieved by the electrospray process.

Significantly, better-aligned graphene by electrostatic force can not only regulate the zinc electrodeposition but also lower the HER catalytic activity, which may result from less edge exposure since the edge is generally regarded as catalytic sites (*45–47*). As illustrated in Fig. 3D, the HER current density of the EG@CF is much lower than that of blank CF and DG@CF, which are more disordered. Suppressing HER is of great importance to the zinc electrodeposition process because: (i) HER has a negative influence on the overall efficiency of the Zn electrodeposition process since the reduction of hydrogen ions is ineffective and (ii) because of the hydrogen ion reactions—the left OH^- reacted with the Zn deposits, resulting in the formation of nonconductive ZnO layers, which, on one aspect, affects the interfacial ion transportation and, on the other aspect, leads to the coarse Zn electrodeposition morphology and, quickly, to the failure of the whole battery. In the blank CF surface, high-intensity signals of ZnO peaks were observed after 20 cycles (Fig. 3E), proving that side reactions (HER) lead to the generation of a large number of side products. Because of the high ratio of ZnO after cycling (fig. S2), the morphology of Zn electrodeposition is coarse and porous (fig. S3) and covers the whole surface of the CF. In stark contrast, the ratio between Zn deposits and ZnO layers after 20 cycles remains low (Fig. 3E and fig. S2) in the EG@CF surface, which is consistent with the HER current results.

On the other hand, to prove the interfacial Zn—C (graphene) bonding at the EG@CF surface, x-ray photoelectron spectroscopy (XPS) was performed. As shown in fig. S4, no C—Zn peak was detected on the surface of Zn deposits ($1 mA·hour/cm^2$) in the EG@CF, meaning that the interfacial metal-substrate bond was not exposed, while a clear C—Zn peak appeared after sputtering the Zn deposits. The C—Zn peak is located at 283.374 eV, which is consistent with the previous report (*48*). The results show that the interfacial C—Zn bond
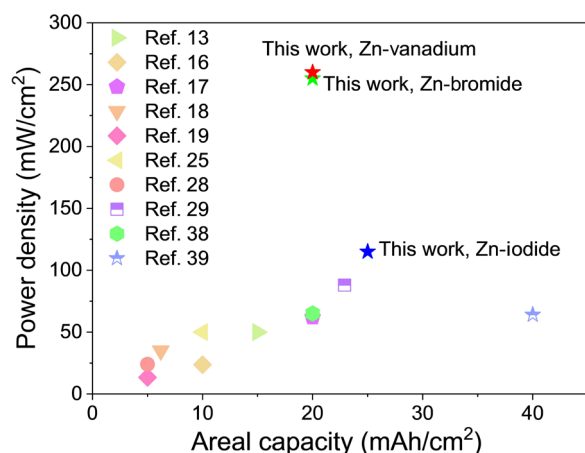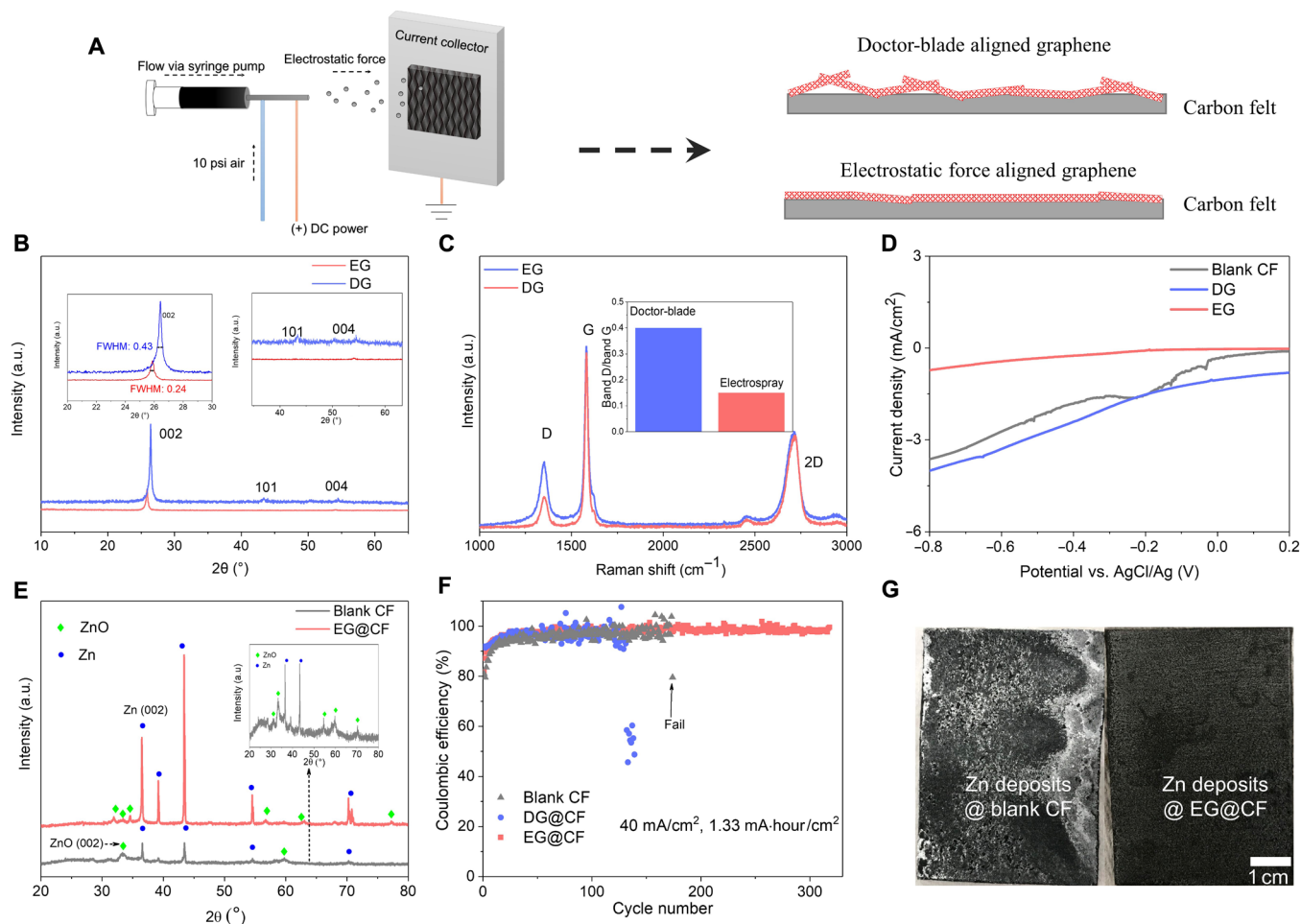
Fig. 3. Interfacial designing for zinc sides. (**A**) Schematic illustrating the electrospray process and how it is used to manufacture textured graphene coatings that enable reversible zinc electrodeposition. (**B**) XRD pattern obtained for graphene coatings produced by the standard "doctor-blade" method, compared to those fabricated using our electrospray methodology. Inset is an amplification of the (101) and (004) planes to illustrate the relative selectivity of the crystallinity obtained for graphene coatings produced by the electrospray methodology. (**C**) Raman spectrum for graphene coatings fabricated by the doctor-blade and electrospray methodologies. Inset is the ratio between the D and G bands. (**D**) Current density versus potential scan illustrating how the HER current varies when the substrate is blank CF, DG@CF, and EG@CF. (**E**) XRD analysis of Zn deposits after cycling at the surface of blank CF and EG@CF. (**F**) CE of blank CF, DG@CF, and EG@CF. (**G**) The Zn deposition morphology at the surface of blank CF and EG@CF after cycling 10 cycles. 40 mA/cm^2, 20 mA·hour/cm^2. a.u., arbitrary units.

indeed exists as we expect and may have good control over the reversible Zn electrodeposition processes. Plating/stripping CE of Zn deposits can further prove the good reversibility of 3D EG@CF substrate under high current density. As Fig. 3F shows, compared with the CE and cycling life of the blank CF (98%, 150 cycles) and DG@CF (98.5%, 120 cycles), the average CE of EG@CF reaches 99.5% and can stably cycle over 300 cycles. The plot of voltage-areal capacity shows the stability of the Zn electrodeposition using the EG@CF (fig. S5). Moreover, unlike blank CF, which shows coarse, dendritic Zn electrodeposition morphology at high current density (fig. S3), Zn deposit morphologies in the EG@CF are uniform at different cycles (10th, 20th, 30th, and 50th) as shown in fig. S6. Even at the large-scale CF (35 cm^2) (Fig. 3G), unlike coarse and nonuniform Zn deposits in the CF surface, Zn deposits in the EG@CF are uniform and smooth over the whole surface, which benefits from the introduction of interfacial metal-substrate bonds. Furthermore, we found that the thickness of the EG layers should be around ~1 μm to avoid all the problems mentioned above (e.g., blocking pores and exposing

edge). Increasing the thickness of EG layers leads to the low CE for full Zn-iodine flow batteries (fig. S7). Together, we can conclude that most of the problems including side reactions and dendrite can be solved and high stability Zn anode in flow battery can be achieved at the better-aligned graphene interphase (EG@CF).

Adsorption process at cathode side

The reaction at the cathode is generally regarded as the limiting step that determines the overall performance of a flow battery when operated at a high current density (*40*). Here, we first choose I$^-$/I$_3^-$ iodine cathode as a validation example to explore the problems at a high current density and design a suitable cathode interface. Then, these general interface–designing principles are extended to all AZFBs, all of which can achieve high power density, high areal capacity, and good stability. For iodine cathode, as illustrated in Fig. 4A, the cathode side with blank CF can only work within a few cycles at a current density of 80 mA/cm^2 or cannot work at 100 mA/cm^2. To diagnose the underlying problems of the iodine reaction process, we first cycled
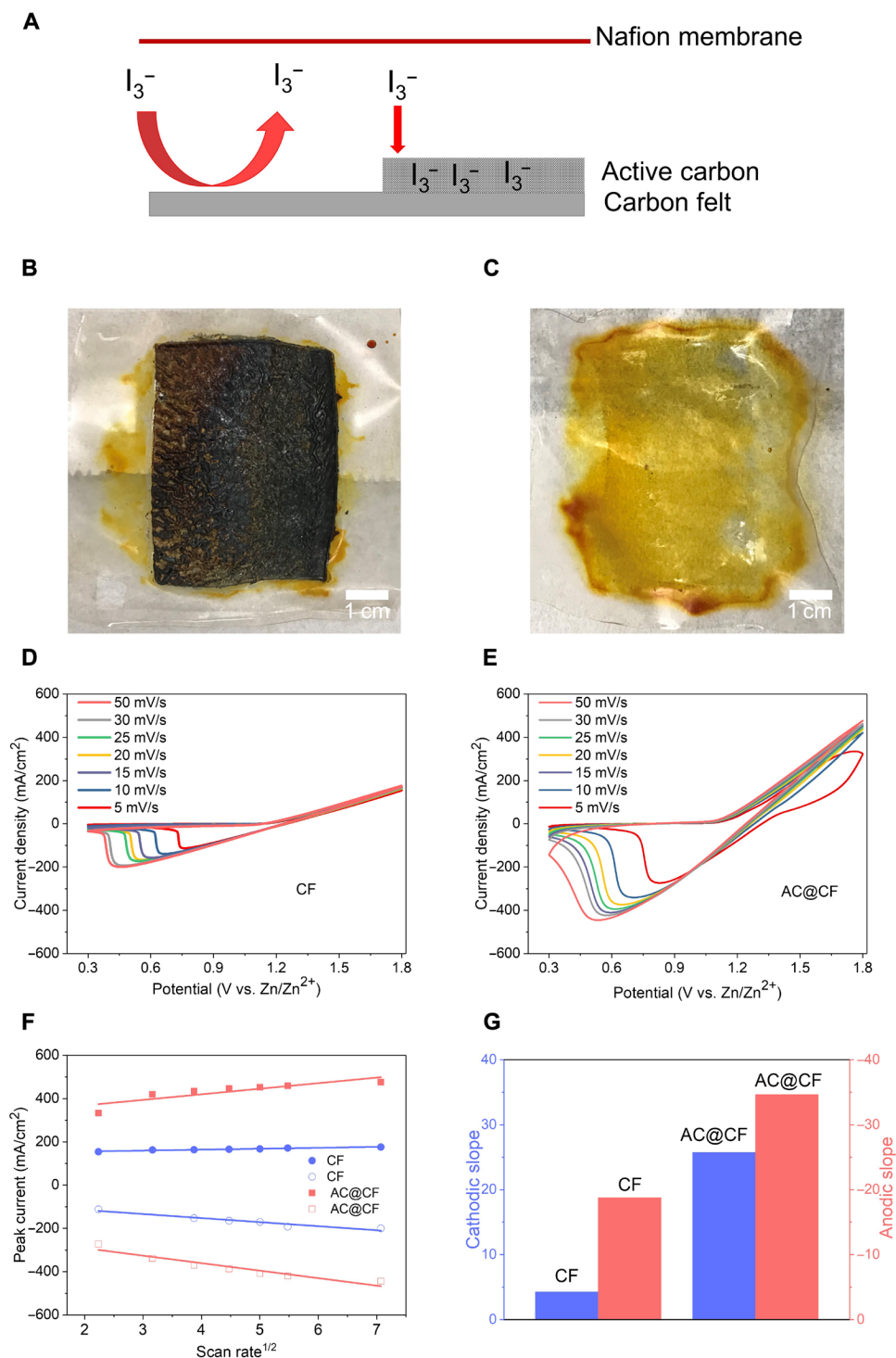
Fig. 4. Interfacial designing for cathode sides. (**A**) Scheme illustrating the design principles for limiting the loss of cathode reaction products. The Nafion membrane surface morphology after cycling with (**B**) blank CF and (**C**) AC@CF. Cyclic voltammetry of Zn-I_2 full battery with (**D**) blank CF and (**E**) AC@CF. (**F**) Peak current density versus scan rate$^{1/2}$ extracted from (D) and (E). (**G**) Values of the anodic and cathodic current slopes extracted from (F).

the flow battery at 80 mA/cm^2 for a few cycles and then opened the flow battery. As shown in fig. S8A, the voltage polarization gradually increased during the charge and discharge processes in the first few cycles, which means that the resistance kept increasing during

the cycling. Unexpectedly, solid iodine was found to cover the whole Nafion surface (Fig. 4B), which may result in the quick failure of the whole battery. To further evaluate this assumption, we removed a slice of the solid iodine on the membrane surface and reran the full

battery cell. It was observed that cells run normally at low current density (fig. S8B), and postmortem analysis indicated that the electrode reactions occur dominantly at the sections of electrode with the iodine layer removed, proving our assumption that the accumulation of solid iodine led to the premature battery failure (fig. S9). Because of the non–ion-conductive nature of the solid iodine covering, the battery would be disconnected after the Nafion membrane was completely covered. This kind of membrane cover results from the fast interfacial reaction rate at the cathode electrode under high current density, but the accumulated products are hard to be adsorbed at the electrode surface and have the propensity to be absorbed into the Nafion surface. Last, the Nafion membrane is totally covered by the product. In summary, on the basis of all results, for the I^-/I_3^- reaction process at high current density, the interfacial reaction should include two steps: step 1, $3I^- + 2e^- \rightarrow I_3^-$; step 2, $I_3^- \rightarrow$ solid iodine. I_3^- mainly comes from step 1. If the generated I_3^- cannot be fixed at the cathode surface, as the electrolyte concentration of I_3^- increases, then the I_3^- will deposit at the preferred surface, such as the Nafion membrane. On the other hand, if I_3^- can be fixed at the cathode surface, as the interfacial concentration of I_3^- increases, then I_3^- will deposit at the cathode surface as solid iodine (fig. S9). Hence, for the cathode side, interfacial adsorption, for both reactant and product, is the key point, especially for high current density.

To investigate the interfacial adsorption problems, AC with high surface area is used. For this purpose, an electrospray approach was used to create a smooth AC coating at a 3D CF cathode surface (AC@CF). Likewise, we noted that a coarse coating by the doctor-blade process would plug the holes of the 3D electrode, further affecting the flowing efficiency (fig. S1). First, we found that the

AC@CF electrode can work at high current densities of 80 and 100 mA/cm^2, meaning that the solid iodine problem may be solved. After 10 cycles, we opened the flow battery and found that there is no solid iodine on the Nafion membrane surface (Fig. 4C). To further see the influence of AC on the interfacial reaction process, cyclic voltammetry (CV) was performed. As shown in Fig. 4 (D and E), compared with the blank CF, the electrode capacity, which is related with the surface area at each scanning cycle, highly increases, meaning that the increased surface area can provide more adsorption and reaction sites for the iodine oxidation/reduction process. The diffusion coefficient, which is extracted from different scan rates, is higher at the AC@CF surface than that of blank CF surface (Fig. 4, F and G), which should also benefit from the strong interfacial adsorption of the reactants and products. Electrochemical impedance spectroscopy (EIS) experiments at different cycles can also prove the stability of improved electrode (EG@CF and AC@CF) (fig. S10). Until here, by analyzing the problems of both anode and cathode sides, our interfacial engineering works are constructed. On the basis of these interfacial surface designs, we can solve the problems mentioned above for anode and cathode sides, respectively. To further prove the effectiveness of these designing principles, the overall performance of the whole flow battery system and different kinds of flow batteries needs to be verified.

Aqueous zinc flow batteries
Figures 5 and 6 report the main results of the present study. Figure 5A shows the good rate capability of the Zn-iodine flow battery with aligned graphene (EG@CF) and AC coating (AC@CF). Significantly, the discharge voltage can maintain high even at a high current density of 100 mA/cm^2 (fig. S11), meaning that high power density is possible
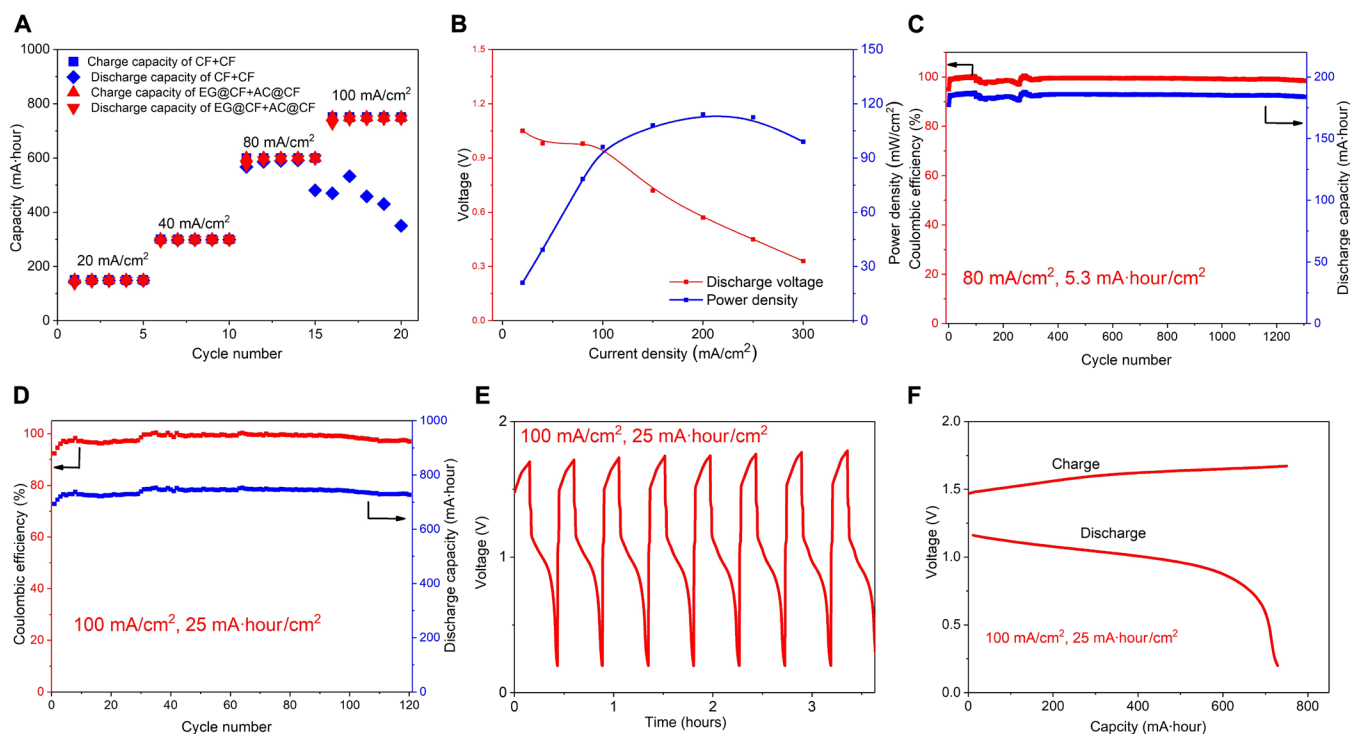
Fig. 5. Electrochemical performance of aqueous Zn-iodine flow batteries. (**A**) Capacity versus cycle number at different rates for Zn-iodine low batteries with blank CF and EG@CF+ AC@CF. (**B**) Average discharge voltage and power density at different current densities were obtained using EG@CF+ AC@CF electrodes. Cycling performance of EG@CF+ AC@CF electrodes at (**C**) 80 mA/cm^2, 5.3 mA·hour/cm^2 and (**D**) 100 mA/cm^2, 25 mA·hour/cm^2. (**E**) The voltage-time curve of (D). (**F**) The voltage-capacity curve of (D).
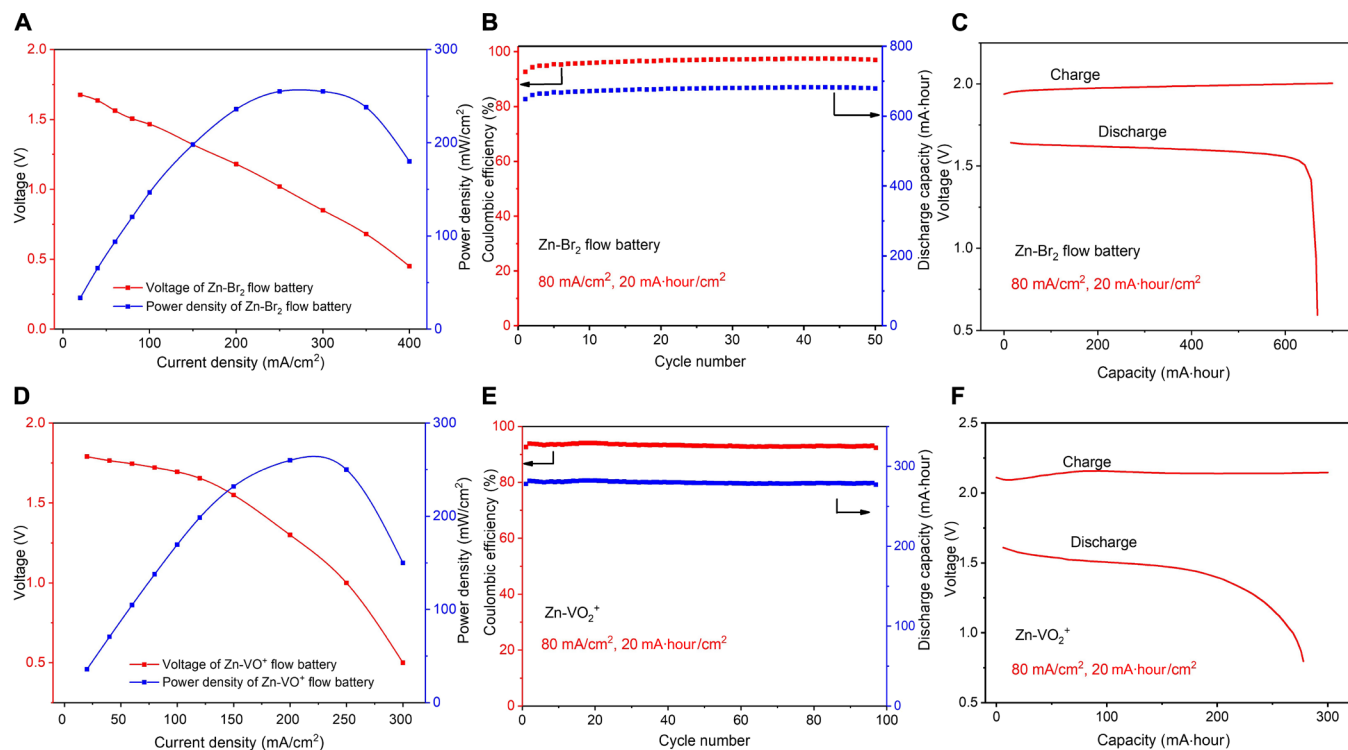
Fig. 6. Electrochemical performance of Zn-bromine and Zn-vanadium flow batteries with EG@CF+ AC@CF electrodes. (**A**) Power density of Zn-bromine flow batteries at different current densities. (**B**) The cycling performance of the Zn-bromine flow battery. (**C**) The capacity-voltage curve of the Zn-bromine flow battery. (**D**) Power density of Zn-vanadium flow batteries at different current densities. (**E**) The cycling performance of the Zn-vanadium flow battery. (**F**) The capacity-voltage curve of the Zn-vanadium flow battery.

here. As Fig. 5B shows, the highest power density of 115 mW/cm^2 for a Zn-iodine flow battery is achieved through interfacial designing. On the other hand, high areal capacity and cycling stability are other essential considerations for practical application. Significantly, at a current density of 80 mA/cm^2, the cycle time with the areal capacity of 5.3 mA·hour/cm^2 is over 1200 cycles (Fig. 5C). In stark contrast to the systems of blank CF electrodes and DG@CF (fig. S12), the Zn-iodine flow battery with the interphase of better-aligned EG@CF and AC@CF shows good stability (over 120 cycles) and high CE (99.2%) at a current density of 100 mA/cm^2 and an areal capacity of 25 mA·hour/cm^2 (Fig. 5D and fig. S13A). The voltage and current density profile confirm the stability of the battery cycling (Fig. 5, E and F, and fig. S13B). The energy density of the improved Zn-iodine flow battery system can reach 200 Wh/L$_{catholyte}$ (fig. S14). Together, high-performance Zn-iodine batteries with high power density, high areal capacity, and good cycling stability were achieved by interfacial designing.

To further illustrate the general utility of the interfacial designing principles, zinc-bromine and Zn-vanadium batteries were further used here. For the latter battery system, considering the high cost of all vanadium batteries (V$_2$O$_5$, 21.38 USD/kg), the replacement of Zn will modestly lower the cost of the whole battery system (*9*, *37*, *49*). Notably, the results reported here for Zn-vanadium batteries are meant to be illustrative—more work is required to improve this system for practical application. For example, considering the acidic environment on the vanadium side of the cell, the proton crossover problem might be addressed via a buffering chamber. By analogy to the design of the zinc-iodine battery system, high discharge voltages

can also be maintained under high current density (fig. S15). Therefore, high power density can be achieved at both zinc-bromine (255 mW/cm^2) (Fig. 6A) and Zn-vanadium (260 mW/cm^2) (Fig. 6D) batteries with the designed interface, respectively. Compared with the blank CF electrode (fig. S16), good cycling stability (Fig. 6, B and E) and high areal capacity (Fig. 6, C and F) were also confirmed at these extended battery systems with better-aligned graphene layers + AC (EG@CF and AC@CF). The energy densities for zinc-bromine and Zn-vanadium battery are 282 and 56 Wh/L$_{catholyte}$, respectively (fig. S14). Since we used single-side flow batteries here, which only flow the anolyte, the high discharge of depth was achieved in all AZFB systems (fig. S17). Hence, we concluded that by rationally designing the interphase at the 3D electrode surface, high-performance AZFBs can be designed and meet the requirements of practical applications, which pave the way for the further development of AZFBs.

DISCUSSION
In summary, we reported the designing principles for high-performance AZFBs in terms of anodes and cathodes. For anode sides, introducing metal-substrate bonding can regulate the Zn electrodeposition morphology and suppress side reactions. For cathode sides, increasing the interfacial adsorption ability is the key point that influences the reaction and cycling process. Electrospray, which is a mature industrial technology, can accommodate the designing principles for 3D electrodes used in flow batteries. Electrostatic force can not only create better-aligned graphene interphase but also control the coating amount and uniform morphology. However, electrode interface

designing can only regulate the interfacial properties, which means that the ion movement in the electrolyte still limits the performance of the flow battery at high current densities, such as energy efficiency. Membrane designing with high ion conductivity is another important point, which has been stressed in some recent works (*15*, *29*).

MATERIALS AND METHODS

Materials

Zn foil (99.97%), $ZnBr_2$, ZnI_2, KI, KCl, $VOSO_4$, H_2SO_4, graphene, and AC were purchased from Sigma-Aldrich. Carbon black Super-P was purchased from TIMCAL. Deionized (DI) water was obtained from Milli-Q water purification system. The resistivity of the DI water is 18.2 megohm·cm at room temperature. Free-standing interwoven carbon fibers (plain carbon cloth 1071 HCB) and CF were purchased from the Fuel Cell Store. The Nafion 115 were purchased from Dupont.

Preparation of electrolytes

For electrodeposition and battery performance characterization, $ZnBr_2$ and ZnI_2 were dissolved in DI water to prepare 3 M electrolyte.

Preparation of electrospray ink

The anode conductive ink was graphene-dissolved in DI water, and the cathode ink consisted of four primary components—AC, carbon black Super-P (TIMCAL), 20 weight % (wt %) of Nafion dispersion (Ion Power), and DI water. The Nafion dispersion acted as a binder and a good surfactant to mix the carbon in water. It was found that the best anode ink composition was 4 wt % of graphene and 96 wt % of DI water, while the best composition for cathode was 1.5 wt % of AC, 0.5 wt % of super-P, 10 wt % of Nafion dispersion, and 88 wt % of DI water. The ink was then ultrasonicated for 60 min before use to remain well dispersed.

Electrospray processing condition

The ink solution was then switched to different 5-ml syringes with a needle (tube gauge, 10; shell gauge, 17). Ten pounds per square inch gauge of air was applied through the shell of the needle, while the pump (Harvard Apparatus) pushed the syringes to spray the solution out. The current collector we used was 5-mm by 7-mm CF (C200, AvCarb, 6 mm in thickness). The distance between the needle and the CFs was 10.5 cm. For cathode treatment, the best amount of solution was 405 μl in total, which was 45 μl for each spray spot. The flow rate was set to 0.015 ml/min. The total amount of solution for anode was strictly limited to 360 μl, which means 60 μl for each spot, and the flow rate was 0.02 ml/min.

Electrochemical measurements

Galvanostatic charge/discharge performance of half cells in coin cell was tested on Neware battery test systems at room temperature. Electrochemical studies were performed using CR2032 coin cells. The area of electrodes in this study is 1.98 cm^2. Zn half cells were assembled using a Zn foil and a 3D CF separated by a glass fiber (GF/A, Whatman), and 50 μl of ZnI_2 electrolyte (3M) was used here.

For all flow battery systems, we used single flow battery systems, in which only the anolyte is flowing through the electrode with the flow rate of 20 ml/min and the catholyte is stationary. This kind of design can improve the utilization of the catholyte. All catholyte volume that we used here was 4 ml, except for the vanadium system, which was 8 ml.

In the Zn/I_2 flow battery, the anolyte and the catholyte were both 6 M KI and 3 M $ZnBr_2$. CFs were current collectors on both sides. For the Zn/Br_2 flow battery, the electrolyte was a combination of 3 M KCl and 2 M $ZnBr_2$. The effective area of the electrode was 35 cm^2 (5 cm by 7 cm). In the Zn-vanadium flow battery, the anolyte was 2 M $ZnBr_2$ and 3 M KCl, while the catholyte was 1 M $VOSO_4$ in 4 M H_2SO_4. The effective area of the electrode was 15 cm^2 (3 cm by 5 cm). The commercially available cation exchange membrane (Nafion 115, Dupont, USA) was used as the separator. The Nafion 115 membranes were treated with 5% H_2SO_4 under 100°C for 2 hours and then washed with DI water at 100°C for 1 hour.

The catholyte of the flow battery would be prepumped into the cathode side and then blocked with pipes, and then 40 ml of electrolyte would be circulated as anolyte. The electrode we used was C200 (AvCarb, 6 mm in thickness), and the separator was Nafion 115 (Ion Power). For Zn/I_2 flow battery, the charging settings were 15 min and 3 A, and discharge settings were 0.2 V and 3 A. For both charge and discharge processes, the current density would reach 100 mA/cm^2, and the areal capacity would reach 25 mA·hour/cm^2. In the Zn/Br_2 flow battery, the charging settings were 15 min and 2.8 A, and discharge settings were 0.6 V and 2.8 A. The battery could reach a current density of 80 mA/cm^2 and an areal capacity of 20 mA·hour/cm^2. For the Zn-vanadium flow battery, the charging settings were 15 min and 1.2 A, while the discharge settings were 0.8 V and 1.2 A. The battery could reach a current density of 80 mA/cm^2 and an areal capacity of 20 mA·hour/cm^2 for both charge and discharge processes.

Characterization of materials

Field-emission scanning electron microscopy was carried out on Zeiss Gemini 500 scanning electron microscope equipped with Bruker energy dispersive spectroscopy detector to study the electrodeposition morphology of Zn. Powder XRD was performed on Bruker D8 Advance ECO powder diffractometer with a Cu Kα x-ray source. CV and linear sweep voltammetry was performed using a CH 600E electrochemical workstation. Renishaw inVia confocal Raman microscope is used for Raman tests of electrolytes (excitation wavelength, 785 nm). XPS was analyzed using a Surface Science Instruments SSX-100 ESCA spectrometer with operating pressure ca. 1×10^{-9} torr. Monochromatic Al Kα x-rays (1486.6 eV) with photoelectrons collected from an 800-μm-diameter analysis spot. Photoelectrons were collected at a 55° emission angle with source to analyzer angle of 70°. A hemispherical analyzer determined electron kinetic energy, using a pass energy of 150 eV for wide/survey scans and 50 eV for high-resolution scans. A flood gun was used for charge neutralization of nonconductive samples. EIS measurements was performed using a Solartron in a frequency range from 7 MHz to 50 mHz with an AC polarization of 20 mV.

REFERENCES AND NOTES

1. D. Lin, Y. Liu, Y. Cui, Reviving the lithium metal anode for high-energy batteries. *Nat. Nanotechnol.* **12**, 194–206 (2017).
2. K. Kodama, T. Nagai, A. Kuwaki, R. Jinnouchi, Y. Morimoto, Challenges in applying highly active Pt-based nanostructured catalysts for oxygen reduction reactions to fuel cell vehicles. *Nat. Nanotechnol.* **16**, 140–147 (2021).
3. M. Park, J. Ryu, W. Wang, J. Cho, Material design and engineering of next-generation flow-battery technologies. *Nat. Rev. Mater.* **2**, 16080 (2016).

4. J. Zheng, M. S. Kim, Z. Tu, S. Choudhury, T. Tang, L. A. Archer, Regulating electrodeposition morphology of lithium: Towards commercially relevant secondary Li metal batteries. *Chem. Soc. Rev.* **49**, 2701–2750 (2020).

5. M. D. Tikekar, S. Choudhury, Z. Tu, L. A. Archer, Design principles for electrolytes and interfaces for stable lithium-metal batteries. *Nat. Energy* **1**, 16114 (2016).

6. Y. Liang, H. Dong, D. Aurbach, Y. Yao, Current status and future directions of multivalent metal-ion batteries. *Nat. Energy* **5**, 646–656 (2020).

7. P. Shi, X.-Q. Zhang, X. Shen, R. Zhang, H. Liu, Q. Zhang, A review of composite lithium metal anode for practical applications. *Adv. Mater. Technol.* **5**, 1900806 (2019).

8. X. B. Cheng, R. Zhang, C. Z. Zhao, Q. Zhang, Toward safe lithium metal anode in rechargeable batteries: A review. *Chem. Rev.* **117**, 10403–10473 (2017).

9. J. Zheng, L. A. Archer, Controlling electrochemical growth of metallic zinc electrodes: Toward affordable rechargeable energy storage systems. *Sci. Adv.* **7**, eabe0219 (2021).

10. TRADING ECONOMICS; https://tradingeconomics.com/.

11. D. E. Turney, G. G. Yadav, J. W. Gallaway, S. Kolhekar, J. Huang, M. J. D'Ambrose, S. Banerjee, Aqueous Mn-Zn and Ni-Zn batteries for sustainable energy storage, in *Energy-Sustainable Advanced Materials*, M. Alston, T. N. Lambert, Eds. (Springer, 2021) pp. 1–26.

12. G. G. Yadav, D. Turney, J. Huang, X. Wei, S. Banerjee, Breaking the 2 V barrier in aqueous zinc chemistry: Creating 2.45 and 2.8 V MnO₂–Zn aqueous batteries. *ACS Energy Lett.* **4**, 2144–2146 (2019).

13. Y. Ito, M. Nyce, R. Plivelich, M. Klein, D. Steingart, S. Banerjee, Zinc morphology in zinc–nickel flow assisted batteries and impact on performance. *J. Power Sources* **196**, 2340–2345 (2011).

14. C.-X. Zhao, J.-N. Liu, J. Wang, D. Ren, J. Yu, X. Chen, B.-Q. Li, Q. Zhang, Zinc-air batteries: A ΔE= 0.63 V bifunctional oxygen electrocatalyst enables high-rate and long-cycling zinc–air batteries. *Adv. Mater. Interfaces* **33**, 2170117 (2021).

15. C. Xie, Y. Liu, W. Lu, H. Zhang, X. Li, Highly stable zinc–iodine single flow batteries with super high energy density for stationary energy storage. *Energ. Environ. Sci.* **12**, 1834–1839 (2019).

16. J. Zhang, G. Jiang, P. Xu, A. G. Kashkooli, M. Mousavi, A. Yu, Z. Chen, An all-aqueous redox flow battery with unprecedented energy density. *Energ. Environ. Sci.* **11**, 2010–2015 (2018).

17. L. Zhang, H. Zhang, Q. Lai, X. Li, Y. Cheng, Development of carbon coated membrane for zinc/bromine flow battery with high power density. *J. Power Sources* **227**, 41–47 (2013).

18. M. Park, E. S. Beh, E. M. Fell, Y. Jing, E. F. Kerr, D. De Porcellinis, M.-A. Goulet, J. Ryu, A. A. Wong, R. G. Gordon, J. Cho, M. J. Aziz, A high voltage aqueous zinc–organic hybrid flow battery. *Adv. Energy Mater.* **9**, 1900694 (2019).

19. C. A. Aubin, S. Choudhury, R. Jerch, L. A. Archer, J. H. Pikul, R. F. Shepherd, Electrolytic vascular systems for energy-dense robots. *Nature* **571**, 51–57 (2019).

20. D. Chao, W. Zhou, F. Xie, C. Ye, H. Li, M. Jaroniec, S.-Z. Qiao, Roadmap for advanced aqueous batteries: From design of materials to applications. *Sci. Adv.* **6**, eaba4098 (2020).

21. G. G. Yadav, J. Cho, D. Turney, B. Hawkins, X. Wei, J. Huang, S. Banerjee, M. Nyce, Going beyond intercalation capacity of aqueous batteries by exploiting conversion reactions of Mn and Zn electrodes for energy-dense applications. *Adv. Energy Mater.* **9**, 1902270 (2019).

22. S. Jin, J. Yin, X. Gao, A. Sharma, P. Chen, S. Hong, Q. Zhao, J. Zheng, Y. Deng, Y. L. Joo, L. A. Archer, Production of fast-charge Zn-based aqueous batteries via interfacial adsorption of ion-oligomer complexes. *Nat. Commun.* **13**, 2283 (2022).

23. J. Zheng, Q. Zhao, T. Tang, J. Yin, C. D. Quilty, G. D. Renderos, X. Liu, Y. Deng, L. Wang, D. C. Bock, C. Jaye, D. Zhang, E. S. Takeuchi, K. J. Takeuchi, A. C. Marschilok, L. A. Archer, Reversible epitaxial electrodeposition of metals in battery anodes. *Sci. Adv.* **366**, 645–648 (2019).

24. J. Zheng, J. Yin, D. Zhang, G. Li, D. C. Bock, T. Tang, Q. Zhao, X. Liu, A. Warren, Y. Deng, S. Jin, A. C. Marschilok, E. S. Takeuchi, K. J. Takeuchi, C. D. Rahn, L. A. Archer, Spontaneous and field-induced crystallographic reorientation of metal electrodeposits at battery anodes. *Sci. Adv.* **6**, eabb1122 (2020).

25. G.-M. Weng, Z. Li, G. Cong, Y. Zhou, Y.-C. Lu, Unlocking the capacity of iodide for high-energy-density zinc/polyiodide and lithium/polyiodide redox flow batteries. *Energ. Environ. Sci.* **10**, 735–741 (2017).

26. J. Zheng, T. Tang, Q. Zhao, X. Liu, Y. Deng, L. A. Archer, Physical orphaning versus chemical instability: Is dendritic electrodeposition of Li fatal? *ACS Energy Lett.* **4**, 1349–1355 (2019).

27. J. Huang, Z. Guo, Y. Ma, D. Bin, Y. Wang, Y. Xia, Recent progress of rechargeable batteries using mild aqueous electrolytes. *Small Methods* **3**, 1800272 (2019).

28. B. Li, Z. Nie, M. Vijayakumar, G. Li, J. Liu, V. Sprenkle, W. Wang, Ambipolar zinc-polyiodide electrolyte for a high-energy density aqueous redox flow battery. *Nat. Commun.* **6**, 6303 (2015).

29. C. Xie, H. Zhang, W. Xu, W. Wang, X. Li, A long cycle life, self-healing zinc-iodine flow battery with high power density. *Angew. Chem. Int. Ed. Engl.* **57**, 11171–11176 (2018).

30. J. Zheng, D. C. Bock, T. Tang, Q. Zhao, J. Yin, K. R. Tallman, G. Wheeler, X. Liu, Y. Deng, S. Jin, A. C. Marschilok, E. S. Takeuchi, K. J. Takeuchi, L. A. Archer, Regulating electrodeposition morphology in high-capacity aluminium and zinc battery anodes using interfacial metal–substrate bonding. *Nat. Energy* **6**, 398–406 (2021).

31. Silicon Products (P) Associates; https://indiamart.com/silicon-product/.

32. G. Deokar, J. Avila, I. Razado-Colambo, J.-L. Codron, C. Boyaval, E. Galopin, M.-C. Asensio, D. Vignaud, Towards high quality CVD graphene growth and transfer. *Carbon* **89**, 82–92 (2015).

33. R. H. J. Vervuurt, W. M. M. E. Kessels, A. A. Bol, Atomic layer deposition for graphene device integration. *Adv. Mater. Interfaces* **4**, 1700232 (2017).

34. A. Jaworek, A. T. Sobczyk, A. Krupa, Electrospray application to powder production and surface coating. *J. Aerosol Sci.* **125**, 57–92 (2018).

35. L. Fei, S. H. Yoo, R. A. R. Villamayor, B. P. Williams, S. Y. Gong, S. Park, K. Shin, Y. L. Joo, Graphene oxide involved air-controlled electrospray for uniform, fast, instantly dry, and binder-free electrode fabrication. *ACS Appl. Mater. Interfaces* **9**, 9738–9746 (2017).

36. M. J. Divvela, R. Zhang, Y. Zhmayev, S. Pinge, J. Hong Lee, S. W. Kima, Y. L. Joo, Control of formation of viscoelastic droplets and distribution of nano-inclusions in functional deposition for lithium-sulfur batteries. *Soft Matter* **15**, 6485–6494 (2019).

37. M. Ulaganathan, S. Suresh, K. Mariyappan, P. Periasamy, R. Pitchai, New zinc–vanadium (Zn–V) hybrid redox flow battery: High-voltage and energy-efficient advanced energy storage system. *ACS Sustain. Chem. Eng.* **7**, 6053–6060 (2019).

38. C. Xie, T. Li, C. Deng, Y. Song, H. Zhang, X. Li, A highly reversible neutral zinc/manganese battery for stationary energy storage. *Energ. Environ. Sci.* **13**, 135–143 (2020).

39. Y. Yin, S. Wang, Q. Zhang, Y. Song, N. Chang, Y. Pan, H. Zhang, X. Li, Dendrite-free zinc deposition induced by tin-modified multifunctional 3D host for stable zinc-based flow battery. *Adv. Mater.* **32**, e1906803 (2020).

40. J. Yang, Y. Song, Q. Liu, A. Tang, High-capacity zinc–iodine flow batteries enabled by a polymer–polyiodide complex cathode. *J. Mater. Chem. A* **9**, 16093–16098 (2021).

41. S. Jin, D. Zhang, A. Sharma, Q. Zhao, Y. Shao, P. Chen, J. Zheng, J. Yin, Y. Deng, P. Biswal, L. A. Archer, Stabilizing zinc electrodeposition in a battery anode by controlling crystal growth. *Small* **17**, e2101798 (2021).

42. J. Zheng, Y. Deng, J. Yin, T. Tang, R. Garcia-Mendez, Q. Zhao, L. A. Archer, Textured electrodes: Manipulating built-in crystallographic heterogeneity of metal electrodes via severe plastic deformation. *Adv. Mater.* **34**, 2106867 (2022).

43. A. C. Ferrari, J. C. Meyer, V. Scardaci, C. Casiraghi, M. Lazzeri, F. Mauri, S. Piscanec, D. Jiang, K. S. Novoselov, S. Roth, A. K. Geim, Raman spectrum of graphene and graphene layers. *Phys. Rev. Lett.* **97**, 187401 (2006).

44. A. Jorio, E. H. M. Ferreira, M. V. O. Moutinho, F. Stavale, C. A. Achete, R. B. Capaz, Measuring disorder in graphene with the G and D bands. *Physica Status Solidi (b)* **247**, 2980–2982 (2010).

45. Q. Yuan, B. I. Yakobson, F. Ding, Edge-catalyst wetting and orientation control of graphene growth by chemical vapor deposition growth. *J. Phys. Chem. Lett.* **5**, 3093–3099 (2014).

46. H. Zhong, T. Wang, Y. Mo, D. Li, C. Zheng, Y. Chen, Three-dimensional stacked graphite sheets with exposed edge-defects as Pt-based catalyst support. *Electrochim. Acta* **404**, 139602 (2022).

47. N. Zhang, W. Ma, T. Wu, H. Wang, D. Han, L. Niu, Edge-rich MoS₂ naonosheets rooting into polyaniline nanofibers as effective catalyst for electrochemical hydrogen evolution. *Electrochim. Acta* **180**, 155–163 (2015).

48. B. T. Gadisa, R. Appiah-Ntiamoah, H. Kim, In-situ derived hierarchical ZnO/Zn-C nanofiber with high photocatalytic activity and recyclability under solar light. *Appl. Surf. Sci.* **491**, 350–359 (2019).

49. LIVE Vanadium Price, News and Articles; https://vanadiumprice.com.

Designing interphases for practical aqueous zinc flow batteries with high power density and high areal capacity

Shuo JinYiqi ShaoXiaosi GaoPengyu ChenJingxu ZhengShifeng HongJiefu YinYong Lak JooLynden A. Archer